ELSEVIER

Contents lists available at ScienceDirect

Earth and Planetary Science Letters

journal homepage: www.elsevier.com/locate/epsl





Seismic full-wavefield imaging of the West Antarctic Ice Sheet interior near the ice flow divide

Zhendong Zhang a,b,*, Nori Nakata b,c, Marianne Karplus d, Galen Kaip d, Lei Qin e, Zhengbo Li f, Caiwang Shi f, Xiaofei Chen f

- a Key Laboratory of Deep Petroleum Intelligent Exploration and Development, Institute of Geology and Geophysics, Chinese Academy of Sciences, Beijing, 100029, China
- b Department of Earth, Atmospheric and Planetary Sciences, Massachusetts Institute of Technology, Cambridge, 02139, MA, USA
- ^c Energy Geosciences Division, Lawrence Berkeley National Laboratory, Berkeley, 94720, CA, USA
- d Department of Earth, Environmental and Resource Sciences, University of Texas at El Paso, El Paso, 79968, TX, USA
- ^e School of Geophysics and Geomatics, China University of Geosciences, Hubei, 430074, China
- f Department of Earth and Space Sciences, Southern University of Science and Technology, Shenzhen, 518055, China

ARTICLE INFO

Editor: H. Thybo

Dataset link: https://ds.iris.edu/mda/2E/#2E_2018-01-01 2019-12-31

Dataset link: https://www.generic-mapping-tools.org/remote-datasets/earth-relief.html

Dataset link: https:// nsidc.org/data/nsidc-0592/versions/1

Keywords: West Antarctica seismic imaging leaky modes englacial reflections

ABSTRACT

The properties and behavior of the West Antarctic Ice Sheet through time are key to understanding climate and sea level change in the near future. We analyze different types of seismic waves from an active-source acquisition deployed on the West Antarctic Ice Sheet and uncover the internal structures of the ice sheet using seismic imaging methods. Surface waves including leaky and normal modes are separated from englacial and bed reflections using a cross-component matched filter method. Leaky modes are uniquely strong in the data possibly due to the firn layer and ice compaction. We use a joint inversion of leaky and normal surface waves for P- and S-wave velocity estimation in the near-surface and attribute the ultra-low Vp and Vs ratios to the pore closure. We observe englacial reflections down to 50 Hz and bed reflections with multiple branches. Such reflection waves are further used to calculate the seismic images of discontinuities in the ice sheet and the bedrock, revealing multiple layers within the ice near the bed and a heterogeneous bedrock with a rugged surface and possibly existing faults. The fine structure of the ice sheet revealed by seismic data helps with searching for possible drain points and evaluating the instability of the ice sheet. Our data analysis shown in the study is also applicable to typical data sets collected for critical zone exploration.

1. Introduction

The West Antarctic Ice Sheet (WAIS) is largely below sea level and therefore could be unstable. In the past interglacial periods, the WAIS completely disappeared (Scherer et al., 1998), and the melted ice could lead to sea levels about 3 m higher than at present (Bamber et al., 2009). In glacial periods, the WAIS extended to the edges of the continental shelf and was drained by ice streams. Pine Island Glacier and Thwaites Glacier discharge much of the ice and sediment from the WAIS and affect thermal and saline ocean circulation (Joughin et al., 2009). Geodetic and geophysical observations have revealed the surface and internal structures of ice and sedimentary layers and advanced our understanding of ice dynamics and their response to climate change (Bentley, 1975; King et al., 2010; Fu et al., 2021a; Wiens et

al., 2022). Radar and seismic surveys are two comparable geophysical methods that have been used to determine the thickness of ice and bed topography. While radar methods can cover large areas in a short time on airborne platforms, they often see only the bed (Eisen et al., 2015). Seismic surveys, especially those using active sources, can provide high-resolution images of englacial structures within the deep ice and physically meaningful model parameters such as P- and S-wave velocities and seismic impedance discontinuities (Horgan et al., 2011).

Seismic waves, which travel through the shallow and deep ice cover, contain a wealth of information about the velocities and discontinuities of ice and the bedrock that can constrain the structure of glaciers, the rate of melting and the ice flow (Zhang et al., 2022). Seismic studies in Antarctica can be categorized into passive-source and active-source studies, depending on the availability of controlled seismic sources

E-mail address: zdzhang@mail.iggcas.ac.cn (Z. Zhang).

^{*} Corresponding author.

such as explosives, vibroseis, accelerated weight drop, seismic gun, and sledgehammer sources. Passive sources such as earthquakes, oceanic waves and human activities are less logistically challenging and sometimes more environmentally friendly compared to active sources, but they also have limitations in their use for seismic imaging. Earthquakes that happened at plate boundaries are far from the stations installed on continental Antarctica and can be used for constraining continentalscale seismic models (Lloyd et al., 2020). Retrieved surface waves from the ambient noise data are often used to invert for shear-wave velocities in the crust or the top 30 meters, depending on the aperture of the seismic array (Shen et al., 2018; Fu et al., 2021b; Zhang et al., 2022). Aside from searching for velocity models, seismologists also use seismic interferometry to estimate anisotropy and internal structures of the ice cap (Pham and Tkalčić, 2021; Chaput et al., 2022). Interferometric processing of ambient noise data is based on cross-correlation of seismic wavefields between receivers. In the case of surface stations, seismic waves having overlapping wavepaths such as surface waves will be reinforced while body waves will be suppressed. Strictly speaking, extraction of Green's function using seismic interferometry requires that the noise sources are distributed homogeneously (Halliday and Curtis, 2008). In practice, seismic interferometry does not retrieve the exact Green's function, which limits its accuracy in resolving wave dynamics, e.g., amplitudes. However, they nonetheless have, historically, provided many important insights into the composition structure of ice sheets (Diez et al., 2014; Shen et al., 2018; Chaput et al., 2022; Zhang et al.,

Seismic waves originating from a single source are often distinct from most of the subsurface noise and thus are easier to monitor (Halliday and Curtis, 2008). In addition, active-source surveys, in practice, can record more complete seismic wavefields including surface waves, diving waves, reflections and free-surface multiples due to the type of sources used. Different types of seismic waves are sensitive to variable model parameters of the ice cap and sedimentary layers. For example, the thickness and velocity structure of the firn layer is better constrained by surface waves than diving waves. Shear waves enable better constraints on the anisotropy of seismic waves in the ice sheet than P waves (Diez et al., 2014). Seismic reflections caused by abrupt changes in seismic impedance retain rich information about the petrophysical properties of subsurface interfaces and thus have been used to estimate the orientation of ice crystal fabric or the mean grain size and to characterize the ice-basal interface (Horgan et al., 2011; Muto et al., 2019; Zhang et al., 2022). Existing seismic studies have assumed that the englacial discontinuities of the ice sheet result from either the incursion of basal materials (Smith, 1996) or abrupt changes in crystal-orientation fabric (Horgan et al., 2011). It is also reported that the instability of the ice sheet is highly dependent on the geometry and characteristic of the bed (e.g., water content) (Parizek et al., 2013; Lai et al., 2020). There have been several active source surveys in the western Antarctic in the past (Bentley, 1971; Peters et al., 2006; Holland and Anandakrishnan, 2009; Horgan et al., 2011; Karplus et al., 2019). Recently, as part of the Thwaites Interdisciplinary Margin Evolution (TIME) project, active-source data were collected by a linear array of three-component seismic nodes (Karplus et al., 2019; Kornei, 2020). The new data sets provide opportunities to recover the fine structures of the ice sheet and the sedimentary layers by applying seismic data processing algorithms developed in recent years (Zhang and Alkhalifah, 2019; Li et al., 2022; Zhang et al., 2022).

In this study, we identify different types of seismic waves including leaky modes, normal modes, diving waves, reflection waves and free-surface-related multiples from the linear array deployed on the ice sheet that recorded active sources. Such seismic waves illuminate the ice sheet from shallow to deep and thus are useful to uncover the interior structures of the ice sheet and the bedrock. Specifically, we estimate the compressional and shear velocities in the near-surface using a joint dispersion curve inversion of leaky and normal modes. The compressional-to-shear velocity ratio indicates a porosity variation with

depth. We then analyze the frequency-dependent response of bed reflections and neighboring englacial reflections from the vertical- and radial-component data. These reflection data are used to seismically image the layer boundaries inside the ice sheet, the ice-basal interface, and deeper sedimentary layers. Our observations, with previous studies, provide new insights of the ice structure as pore closing, crystal size or sharpness of each layer from the surface to the shallow sedimentary layer. We anticipate the wave phenomena and techniques introduced in this study are also applicable to a larger number of ice-based and land-based data sets.

2. Study site

The WAIS represents the portion of the Antarctic ice sheet that covers west Antarctica. As a sea-based ice sheet, its bottom lies below sea level, and its edges flow into floating ice shelves. The WAIS has contributed to a significant loss in ice, and a rise in the sea level, since the start of the 21st century, as a result of the rapid melting, retreating and accelerating of major glaciers (Meredith et al., 2019). Geological and glaciological data were thus collected to examine the asymmetries of the thickness change in the divide. The WAIS Divide ice core data help us to understand the crystal structure of the ice (Fitzpatrick et al., 2014) and the Holocene accumulation rate (Koutnik et al., 2016). Seismic surveys are also carried out to examine the composition of the ice in the vicinity of the WAIS Divide drilling site, which is more cost-effective than deep-ice drilling.

We study the active-source seismic data collected about 5 km northeast of the WAIS Divide Camp along-flow toward the Walgreen Coast. The acquisition line has 36 explosive sources (each 300 grams pentolite) placed in shallow drilled holes (1.3-3.1 m deep) and 76 3-component (3C), Z-land Gen2, 5 Hz Magseis Fairfield seismic nodes buried at 30 cm depth (Ringler et al., 2018). The seismic array is about 2.25 km long with 30 m and 60 m separated nodes and sources, respectively, as shown in Fig. 1. These seismic node configurations were designed to record controlled seismic source tests during January 2019 (Karplus et al., 2019), but they are also very useful for passive seismic studies (Chaput et al., 2022; Zhang et al., 2022). The seismic line used in this study follows the same location as a previous controlled-source seismic reflection line collected in 2008-2009 (Horgan et al., 2011, Figure 1b) and is partially co-located with a radar line collected in 2020 (Young et al., 2021).

3. Separation of surface and reflection waves

We observe a series of seismic waves such as surface waves, reflections and multiples in the common-shot gathers (one of 36 gathers is shown in Fig. 2). Different types of seismic waves travel different paths in the ice sheet and are sensitive to variable subsurface parameters. Surface waves include leaky and normal modes traveling along the free surface and are useful signals for velocity estimation in the near-surface. Reflected waves from englacial reflectors or the bedrock are helpful in imaging seismic discontinuities. However, surface waves often contaminate reflection waves and thus surface-wave attenuation is needed to utilize body waves. Conventional ground-roll attenuation approaches separate surface waves and body waves by examining their different frequency-slowness responses (Wang and Wang, 2017; Zheng and Hu, 2021). Such methods treat the vertical and horizontal component data independently and assume a mild lateral variation in velocity. In fact, with the availability of multi-component data, we may take one component of the recordings as the template surface waves for another. We designed non-stationary matching filters to attenuate surface waves by minimizing the difference of vertical- and horizontal-component data. This idea is supported by the fact that the main difference between the radial and vertical components of the leaky and normal modes is the phase shift (Schröder and Scott, 2001). Technical details and waveform comparisons are provided in the Supplementary Material.

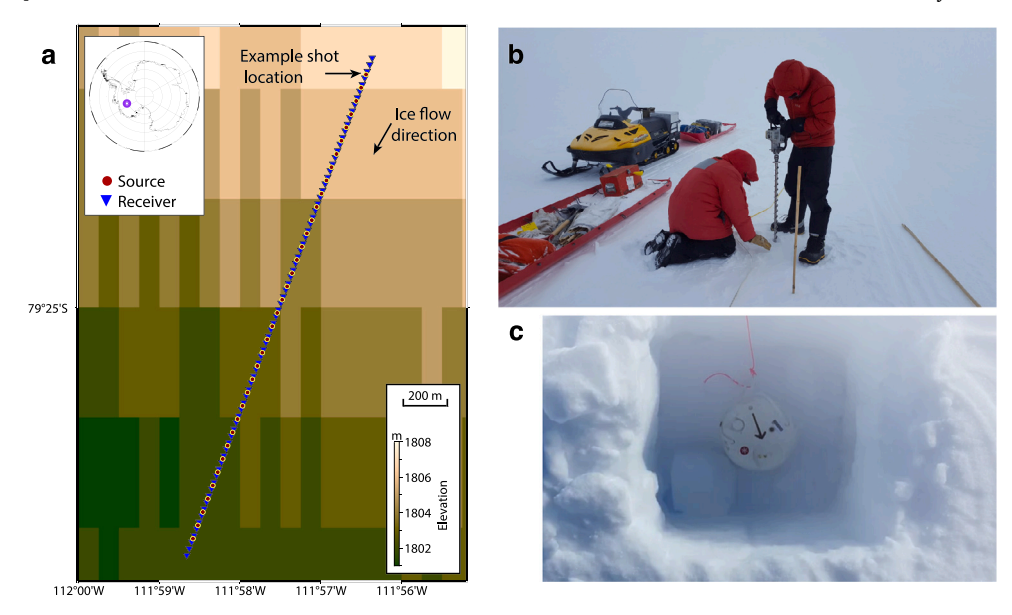


Fig. 1. a) Map of explosive sources and three-component nodes used in this study overlaid with the 15 arc-second global relief (ETOPO, 2022) for the ice surface and b) photos from fieldwork showing a team drilling a hole (less than 5 m) for an explosive source and c) a three-component (3C) Magseis Fairfield seismic node deployed in a 30-cm-deep hole. The array is about 2250 m-long with 76 3C nodes and 36 sources separated by 30 m and 60 m, respectively. We set the receiver located at the northeast corner as the first trace.

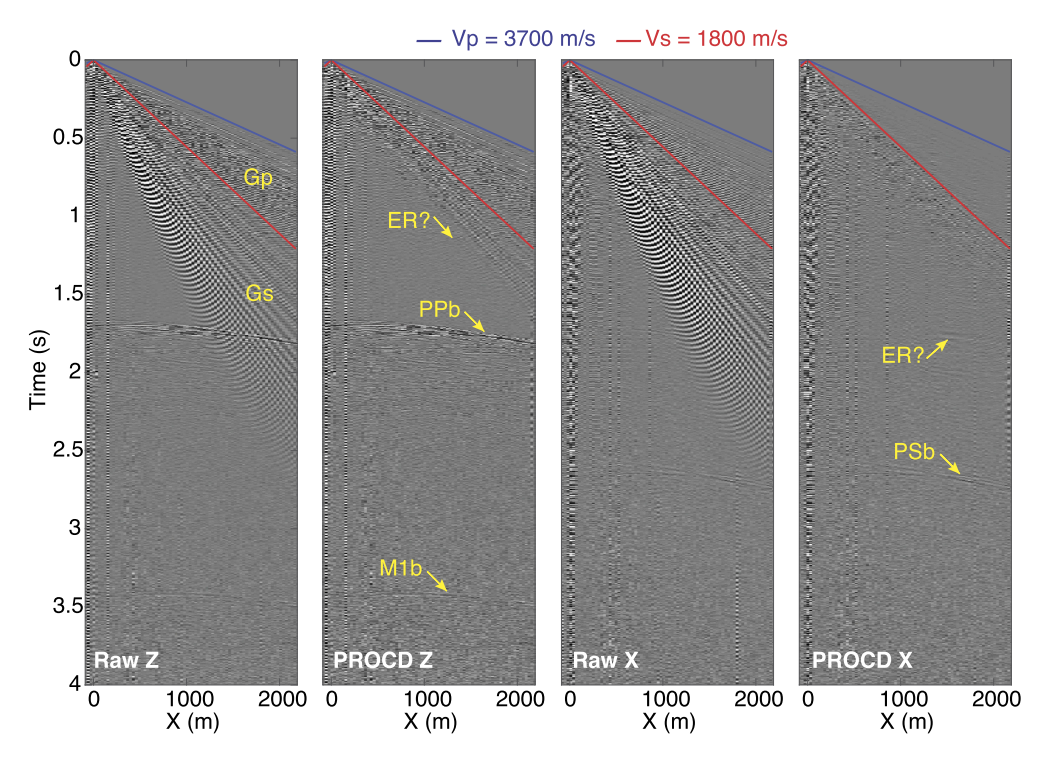


Fig. 2. Example of raw and processed (PROCD) vertical- and radial-component common-shot gathers. We observe strong leaky (Gp) and normal (Gs) modes from the raw vertical- and radial-component recordings. After applying the proposed data processing, we attenuate such surface waves and highlight body waves, such as direct P- and S-waves traveling at about 3700 m/s and 1800 m/s, respectively. Englacial (ER), ice-rock basal interface reflections (PPb and PSb) and their free-surface-related multiples (M1b) are also highlighted.

The processed vertical-component data highlight *PP* reflections from the ice-basal interface previously hidden by surface waves in the far-offset. Similarly, the processed radial-component data also emphasize the converted waves at the ice-basal interface (PSb) and englacial reflections. More importantly, surface waves are greatly attenuated and the first breaks of the primary S-waves distinguish themselves from the background data, which facilitates the traveltime picking of primary S-waves. Waveforms of the preprocessed first breaks are slightly different from the raw data, which may be due to the interference be-

tween the body and surface waves. Nevertheless, the processed data highlight the first breaks of primary P- and S-waves in vertical and radial components and allow robust traveltime picking. We show the shear-to-compressional wave traveltime ratio versus the source-receiver distance in Fig. 3. The ratio of primary (i.e., diving) S- and P-time increases rapidly for source-receiver (S-R) distances smaller than 500 m and stabilizes at around 1.91 (mean value) in mid-to-far offsets, and thus we anticipate that a two-layer model may explain the observed traveltime ratios. The shallow firn layer has a large velocity gradient

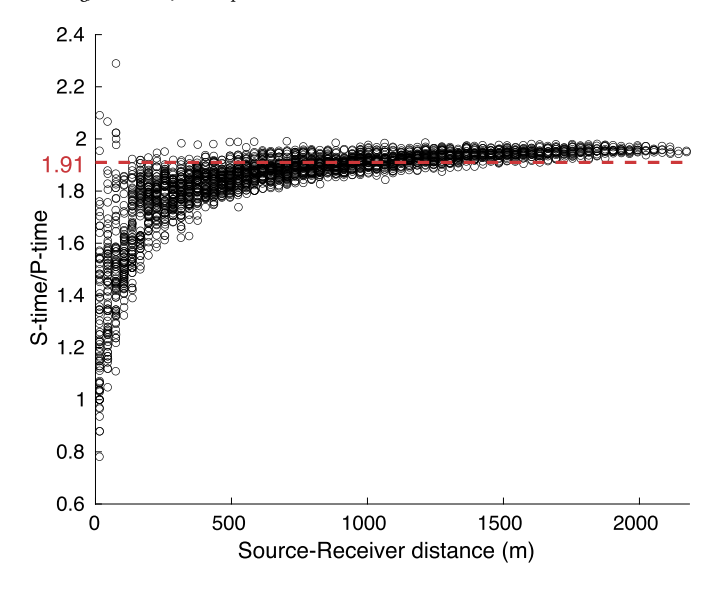


Fig. 3. P- and S-wave traveltime ratios for all source and receiver pairs (2736 picks). They are picked from the processed waveforms and sorted into ascending source-receiver (S-R) distances. The red dashed line indicates the mean value of the P- and S-time ratio (1.91).

with increasing P- and S-wave velocity ratios while the deep ice layer has a more constant P- and S-wave velocity ratio. Such a velocity model revealed by diving waves also agrees with velocity models calculated from the dispersion spectrum inversion of surface waves (Zhang et al., 2022). However, the empirical analysis is not accurate enough to make a quantitative comparison and thus we use a joint inversion of leaky and normal modes for an accurate estimation of P- and S-waves in the near-surface, which will be explained in the following sections.

4. Shallow ice-sheet structure revealed by a joint inversion of leaky and normal modes

Leaky surface waves are a type of wave that travel along a surface and have a phase velocity that falls between the P- and S-waves. They are known to be inhomogeneous and exist only for materials with a Poisson ratio above 0.263 (Schröder and Scott, 2001). Leaky modes are sensitive to shallow velocity changes of P-waves and are useful for constraining P-wave velocities in the near-surface (Oliver and Major, 1960; Gao et al., 2014; Li et al., 2021, 2022). With the previously picked first breaks of primary P- and S-waves, we are able to isolate the potential leaky modes from the raw waveform data. The verticalcomponent leaky surface waves shown in Fig. 4a are overlaid with the picked traveltimes of primary P- and S-waves. To facilitate analysis of data at the desired frequencies, we convolve the raw recording with a Ricker wavelet dominated at 40 Hz. The first breaks are probably diving P-waves, while the later dispersive arrivals are believed to be leaky surface waves formed by post-critical P-wave reflections and refractions at the firn-ice interface (Roth et al., 1998). We also plot the waveforms extracted at different locations for a better comparison in Fig. 4b and the first breaks overlap with picked traveltimes reasonably well. The plot in addition verifies the accuracy of the previously picked traveltimes of diving P-waves. Leaky surface waves are known as dispersive and thus we show their frequency and phase velocity spectrum in Fig. 4c. Three potential dispersion modes are visually identifiable from the plot and we pick the corresponding dispersion curves for velocity inversion in the following sections.

Normal modes or Rayleigh waves have been widely observed and utilized for shear-wave velocity estimation in the near-surface (Xia et al., 1999; Shearer, 2019). Rayleigh waves that emerged from correlations of the ambient noise were reported using the same acquisition line in a previous study (Zhang et al., 2022). In this work, we revisit

Rayleigh waves recorded in an active-source survey. With the previously picked traveltimes of primary S-waves, we can easily highlight possible Rayleigh waves as shown in Fig. 5. These are band-limited signals, which are convolutions of the raw recording with a Ricker wavelet dominated at 20 Hz. Limited by the sparse sampling of receivers and the low velocity in the near-surface, the maximum frequency of measurable Rayleigh waves should be lower than 30 Hz (see Foti et al. (2018) for guidelines). The vertical component of selected waves is dispersive as expected but also shows complex mode conversions right after the first breaks of primary S-waves. For a better comparison, we also plot the waveforms at selected locations in Fig. 5b. The time-series data show a time-dependent variation of the frequency content and clustering of arrivals. The picked traveltime of diving S-waves overlaps with the first breaks of S-waves, which in addition verifies the accuracy of the picked traveltime for S-waves. The dispersion spectra of the verticalcomponent Rayleigh waves are calculated and plotted in Figs. 5c. The fundamental mode is dominant in energy and a potential higher-order mode is also observed from the dispersion spectra. We pick the dispersion curve of the fundamental mode from the vertical-component data and ignore higher-order modes since the target frequency range is reaching or above the limit of data aliasing. Artificial dispersion energies marked by a single arrow are likely caused by data aliasing and thus are ignored.

Shallow structures of the firn and ice layers are often obtained from 1D inversion of Rayleigh and/or Love waves. Only S-wave velocity is well-constrained by normal modes inversion due to the variable data sensitivity. The P-wave velocity can be estimated from primary P-waves or the empirical relation with S-wave velocity. However, primary Pwaves may not penetrate the ice layer due to the strong velocity contrast between the shallow firn and deep ice. The leaky modes, which are more sensitive to perturbations of P-wave velocity, could be used for Pwave velocity estimation in the near-surface. Here we use the previously picked dispersion curves of leaky and normal modes jointly (e.g., Figs. 4 and 5) to invert for 1D P- and S-wave velocity model. Following the work of Li et al. (2022), we simulate the leaky and normal modes using a semi-analytical spectral element method (Shi et al., 2022) and calculate Vp and Vs updates using the Levenberg-Marquardt method (Xia et al., 1999). As we mentioned earlier, Vp and Vs are mainly constrained by leaky and normal modes, respectively, in the proposed joint inversion. Figs. 6a and 6b show the initial and inverted 1D P- and S-wave velocities and their ratios. The starting S-wave velocity was obtained from a 2D wave-equation dispersion spectrum inversion (Zhang et al., 2022) and the starting P-wave velocity is a scaled version (2X) of the S-wave velocity. The newly inverted P- and S-wave velocity model indicates a low-velocity firn-air layer in the shallow (< 12 m) and a firn layer with a large velocity gradient (< 70 m). In comparison, Zhang et al. (2022) estimated the thicknesses of the firn-air layer and firn-layer to be about 17 m and 62 m, respectively, using low-frequency (e.g., 2-20 Hz) ambient noise data. The compressional to shear wave velocity ratio (V_n/V_s) is often used as a key parameter for lithology and fluid prediction (Duffaut and Landrø, 2007). With the relation between V_p/V_s ratios and the differential stress learned from ultrasonic core measurements, the increased V_p/V_s ratio at shallow depth may correspond to the unconsolidated snow layer (e.g., Fig. 6). The accumulation of unconsolidated snow and firn up to about 70 m depth will increase the differential stress and thus result in a decrease of V_n/V_s ratio. With an increased portion of consolidated ice at larger depths, the $V_{\scriptscriptstyle D}/V_{\scriptscriptstyle S}$ ratio is approaching a constant value of standard ice (Wittlinger and Farra, 2012). The ratios of V_p/V_s , calculated from the inverted 1D velocities, in general, agree with the measured P- and S-wave traveltime ratios (e.g., Fig. 3) except for the very shallow layers (e.g., 0-70 m). We trust the calculated V_p/V_s ratios more than the traveltime ratios because of the higher data sensitivity of normal and leaky modes than diving waves at such shallow depths. The synthetic dispersion curves agree well with those calculated from the observed data. The high-order leaky modes are also correctly identified and utilized.

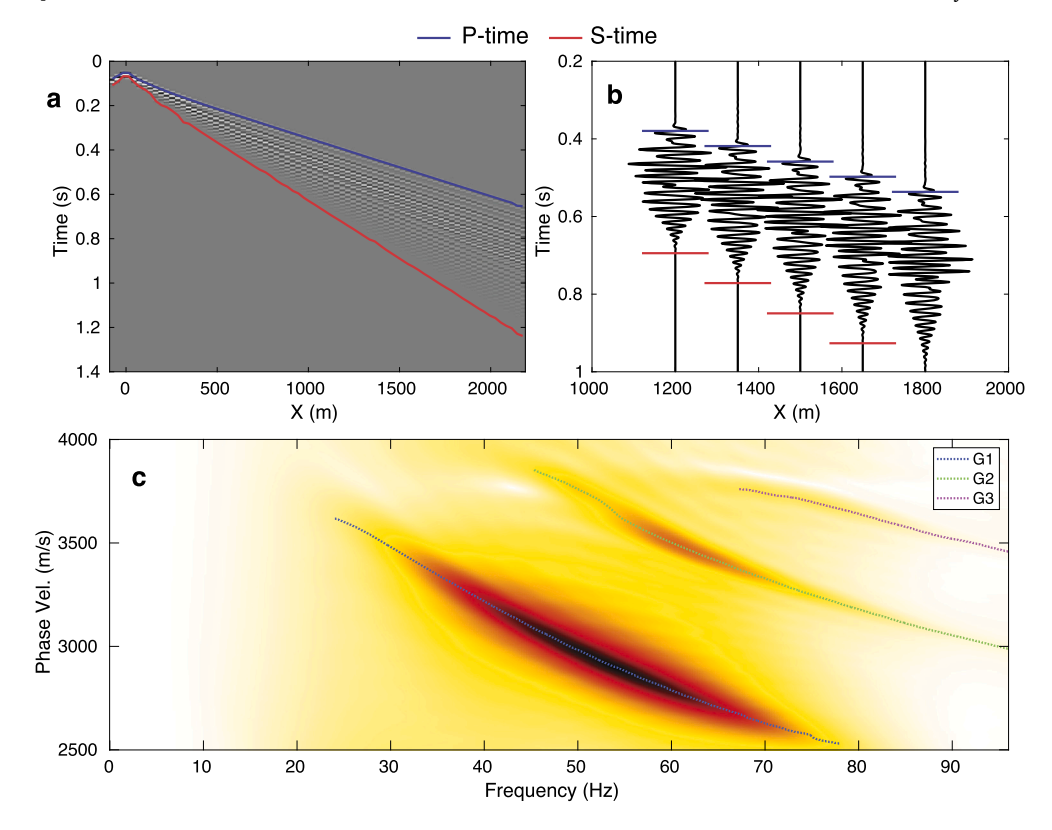


Fig. 4. Windowed leaky modes of the vertical-component data. a) Example common-shot gathers overlaid with picked P- and S-wave traveltimes. b) Trace-by-trace waveforms at selected locations. The picked S-wave traveltime is beyond the maximum plotting time for the last trace and thus is not showing. c) The frequency-velocity spectrum overlaid with picked three leaky modes (G1-G3).

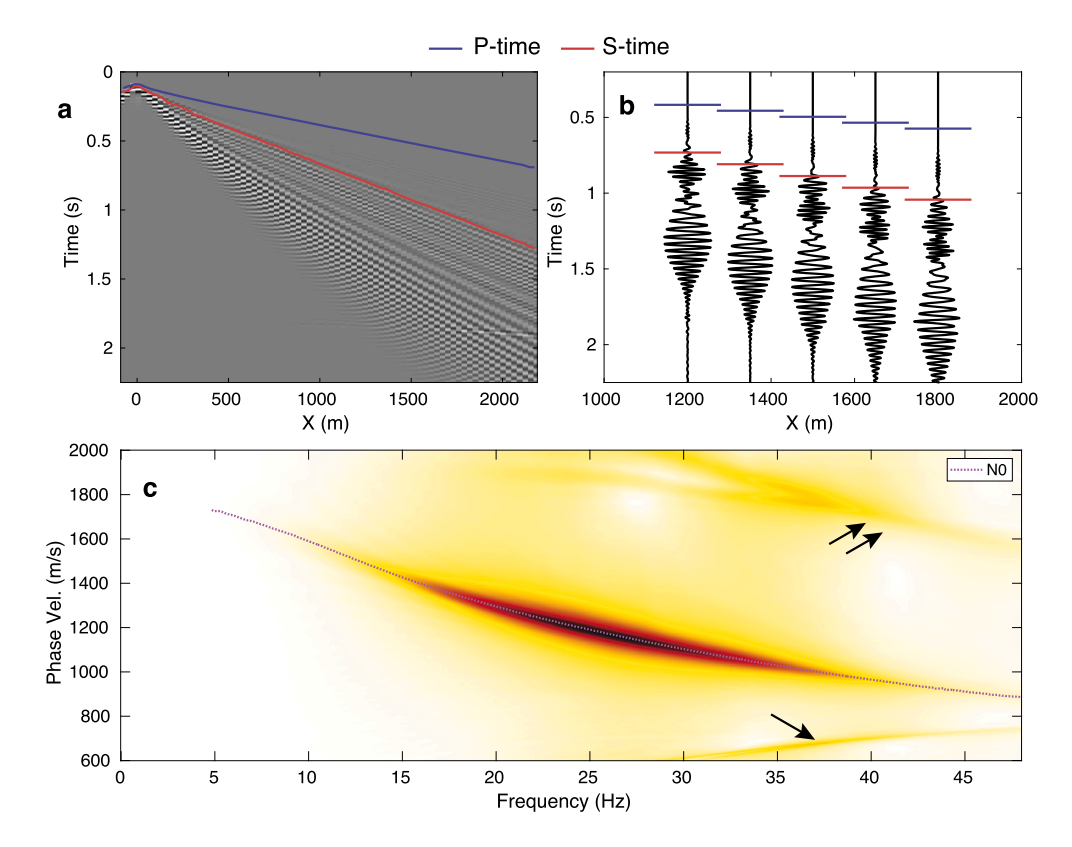


Fig. 5. The vertical component of selected normal modes. a) Example common-shot gathers overlaid with picked P- and S-wave traveltimes. b) Trace-by-trace waveforms at selected locations. c) The frequency-velocity spectrum overlaid with the picked fundamental mode. The single arrow points to the aliased energy due to the sparse receiver sampling. The double arrows may indicate potential higher-order modes.

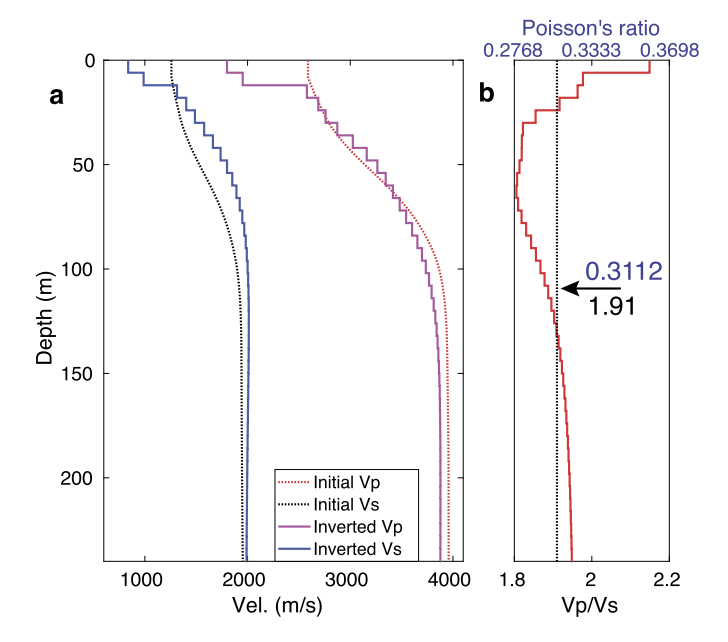


Fig. 6. 1D velocity models. a) P- and S-wave velocity profiles. b) P- and S-wave velocity ratios. Vp and Vs were jointly inverted using the picked dispersion curves from leaky and normal modes, respectively. The dashed vertical line indicates the Vp and Vs ratio of 1.91 or the Possion's ratio of 0.3112. The smooth models from (Zhang et al., 2022) were used as the starting models.

5. Reflection wave analysis and deep-structure

Active-source surveys record high-quality seismic reflections from the englacial discontinuities and the bedrock, which are often not recoverable by crosscorrelation of ambient noise or radio-echo-sounding techniques. Our experiment repeats the active-source survey of the Lline in Horgan et al. (2011) and expands our knowledge about layer boundaries in the target area. In summary, we observe englacial PP and PS reflections at lower frequencies (e.g., 50-100 Hz for PP and 2-50 Hz for PS) and obtain cleaner seismic images of the ice-basal interface and sub-ice materials than existing studies. In Fig. 7, we show the vertical component of seismic reflections and free-surface-related multiples, after applying band-pass zero-phase Butterworth filters. Note that we use surface-wave-attenuated data in the following analysis. Bed reflections have a reasonably broad frequency band (e.g., 2-400 Hz), which is expected for the ice-basal boundary. Multi-pathing bed reflections caused by the topography of the basement are observed (see the Supplementary Material for evidence). Complicated reflections arriving later than bed reflections may indicate a heterogeneous basement. The free-surface-related multiples traveling through the shallow firn layer one more time than primary reflections only exist at lower frequencies (e.g., below 100 Hz) and have a much weaker amplitude. We observe englacial reflections at even lower frequencies (e.g., 50-100 Hz) than an earlier study at the same location (e.g., Horgan et al. (2011)). The englacial reflections do not exist at lower frequencies (e.g., 2-50 Hz), indicating small-scale discontinuities that may cause such reflections. Recent studies have associated such seismic discontinuities with either enclosing basal materials (Smith, 1996) or abrupt changes in crystalorientation fabric (Horgan et al., 2008) and/or grain size (Zhang et al., 2022). The radial-component data, containing mainly converted Swaves, show clear bed reflections at frequencies lower than 100 Hz (see the Supplementary Material). Such converted waves only exist at far offsets and also have weaker amplitudes. The seismic velocity in porous media is constituted of the matrix and fluid velocities (Han et al., 1986), and the substitution of the fluid would result in velocity alterations for P-waves, not S-waves. With reference to such established seismic reactions to petrophysical characteristics in the subsurface, we anticipate that the fluid replacement in the porous ice may cause strong PP and weak PS reflections. There are also some low-frequency (below 50 Hz) englacial-like PS reflections that arrived earlier than the bed reflection. By comparing with the arrival time of the two englacial reflections identified from the vertical component data (e.g., Fig. 7), we conclude that such converted waves should come from shallower englacial reflectors.

We then calculate seismic images of the englacial, ice-basal, and bedrock discontinuities using the reverse-time migration method (Zhang et al., 2022). Reverse-time migration (RTM) maps the time-domain seismic reflections to depth-domain seismic images by back-propagating the surface wavefields to the subsurface location where they were generated. When the velocity model is kinematically accurate, the imaged reflectors will be placed in the correct locations. Since the target area is mostly ice, obtaining a kinematically accurate velocity model for migration is easy. Both the constant ice velocity model (e.g., Vp = 3850 in Horgan et al. (2011)) and the depth-extended inverted velocity model (Zhang et al., 2022) can provide similar seismic migration images (see the Supplementary Material).

We first calculate the RTM image using high-frequency (i.e., 2-200 Hz) data after surface wave removal. As shown in Fig. 8, there are five englacial reflectors imaged within about 700 m above the bedrock, indicating a variation in seismic impedance (e.g., velocity product density) of the ice layers. We further confirm the accuracy of the imaged englacial reflector by comparing with Kirchhoff migration with variable velocities (see the Supplementary Material). The dipping direction of imaged englacial reflectors generally agrees with the bedrock's topography and the ice flow direction. A shallow ice layer is offlapping a deeper one at about 3000 m depth, considering the direction of ice flow. A partial melting of ice near the bedrock might explain the disappearance of the deepest dipping englacial reflector. The imaged englacial reflectors are unlikely caused by the inclusion of basal since they're nearly laterally homogeneous, and seismic anisotropy caused by variations in the c-axis is a possible reason. However, the physical reasons for the c-axis change between layers need further exploration. According to petrophysical responses of reflected P- and S-waves, fluid replacement in layers can cause stronger PP reflections than PS reflections. We anticipate fluid replacement near the bedrock alternates the friction of englacial layers, and ice flow further rearranges the c-axis of

The topography of the ice-basal interface and detailed structures of the bedding rock are further investigated using lower-frequency data. In specific, we use the vertical component of 2-50 Hz processed data (e.g., shown in Fig. 7) as the input wavefield for reverse-time migration (Zhang et al., 2022). The seismic image shown in Fig. 9 shows a clear seismic image of the ice-basal interface centered at around 3340 m. The imaged ice-basal interface has a topography varying from 3440 m (north) to 3240 m (south), sloping downward inland, agreeing with the bed topography based on seismic methods (e.g., Figure 2 in Horgan et al. (2011)), mass conservation, streamline diffusion, and other methods (Morlighem, 2022). The rugged ice-basal interface causes the bright or dimming of reflector images and the triplications of bed reflections, as shown in Fig. 7. However, neither the rugged surface nor a layered bedrock model can generate complicated later reflections observed from the data (see the Supplementary Material). The structural image indicates that the bedrock itself is heterogeneous and faults may exist, agreeing with the geology background that thin sediments or extensive volcanic rocks or intrusions widely exist in West Antarctica (Artemieva and Thybo, 2020; Jordan et al., 2023). Kirchhoff and RTM migration images calculated from variable band-limited reflections and a constant migration velocity and a numerical test also support our finding (see the Supplementary Material).

6. Discussion: structure of the ice-sheet and the basement

Seismic waves recorded by the active-source survey contain rich information about the internal structure and petrophysical properties of the ice sheet and the bedrock. After composing the velocity and struc-

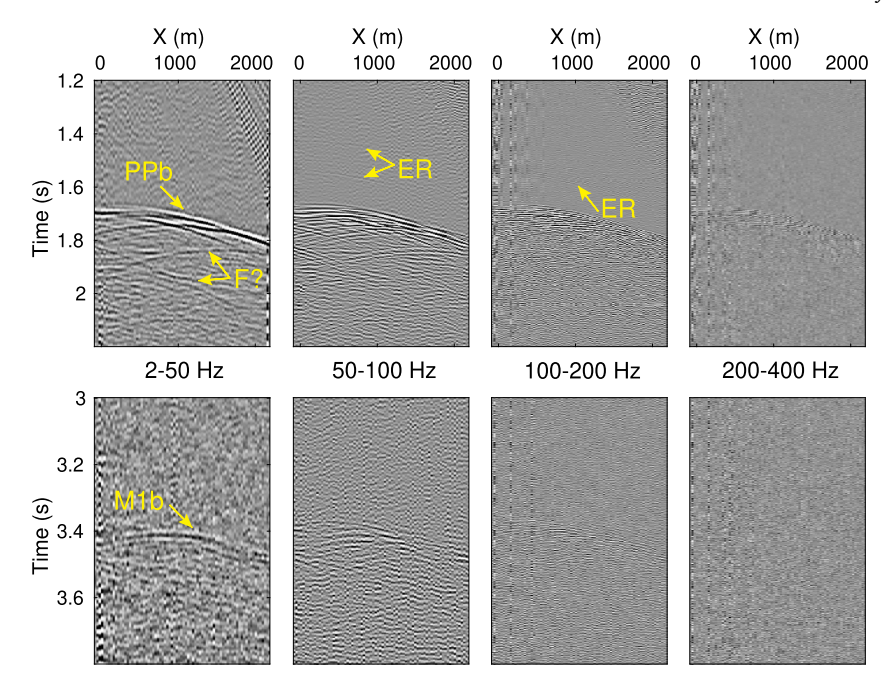


Fig. 7. A zoomed-in view of the vertical-component reflection data, after applying zero-phase band-pass Butterworth filters. The ice-rock basal interface reflections (PPb) show overall flat but rugged features in the wide-bandwidth data (2-400 Hz). Reflections from the rock (geology) beneath the ice are also observable. The free-surface related multiples of the ice-rock basal interface reflections only appear in waveform data below 200 Hz and have lower apparent frequencies than the primary reflections. Several englacial reflections caused by seismic discontinuities in ice are identified at certain frequencies such as 50-200 Hz.

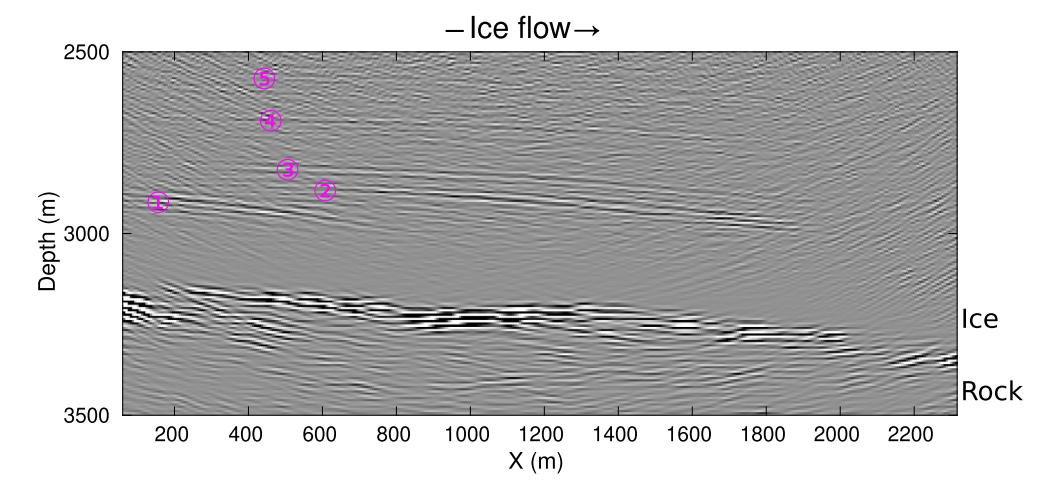


Fig. 8. Reverse-time migration image of the englacial discontinuities. Five englacial reflectors are identified within 700 m above the bedrock, and they're dipping in the direction of the ice flow.

ture information we have in this study and some prior knowledge about the WAIS, we use a sketch plot to show our interpreted structures of the ice sheet and the bedrock in Fig. 10. The compressional and shear velocities estimated from a joint inversion of leaky and normal modes indicate a two-layer model of the near-surface. The calculated V_n/V_s ratio is dependent on the differential stress (Duffaut and Landrø, 2007) and thus is used to infer the depth of unconsolidated and consolidated firn layers. From the 1D velocity models, as shown in Fig. 6, we observe a reduction of V_p/V_s ratios from about 30 m to 70 m depths, which may indicate an increase of the differential stress. The increased differential stress may compact the firn layer and close the pores. Such depth coincides with the firn thickness calculated using the empirical equation (Zhang et al., 2022) and the core analysis (Battle et al., 2011). At greater depths, V_p/V_s ratios gradually increase to those of the ice. We anticipate that the pure ice layer starting from about 120 m depth contains ice crystals with variable grain size and c-axis according to our previous analysis of the SH reflections (Zhang et al., 2022) and other literature works (Horgan et al., 2011; Muto et al., 2019). We exclude the case of basal intrusion that causes such englacial reflections since the imaged reflectors are horizontally continuous and nearly flat. Strong PP and weak PS reflections at these discontinuities indicate that fluid replacement at layers may happen, which will change the friction of ice sheets and further cause variations in the c-axis. The seismic image derived using reverse time migration indicates that the ice-basal interface has a rugged surface (e.g., 3340±100 m), and the bedrock is heterogeneous, in agreement with existing studies in nearby areas (Horgan et al., 2011; Muto et al., 2019; Clyne et al., 2020). Our new results show a much cleaner image of the ice-basal interface than a previous study (e.g., Figure 2 in Horgan et al. (2011)). Previous studies have indicated the existence of subglacial lakes (Siegert et al., 2005) and a lower shear wave velocity in the deep ice sheets (Wittlinger and Farra, 2015). We haven't searched for direct evidence of the presence of liquid water in this study. In our future work, we plan to update the P- and S-wave velocities of the whole ice sheet using reflection waveform inversion

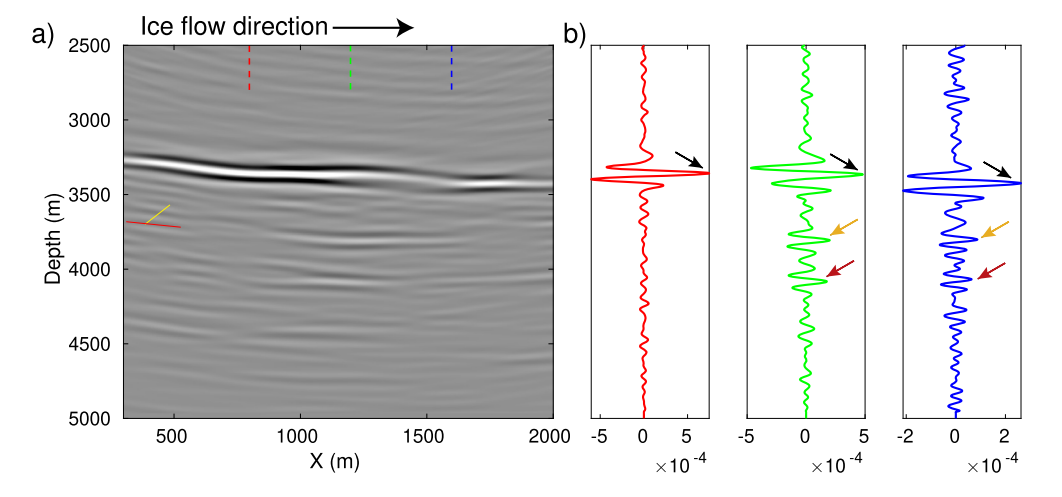


Fig. 9. Reverse-time migration image of the ice-rock and rock discontinuities. a) For the whole array and b) for the selected locations. We use the processed vertical-component data of 36 shots (e.g., data shown in Figs. 2) as the input data. The ice-rock basal interface is coherently reconstructed at all the selected locations while the rock discontinuities are present as local structures.

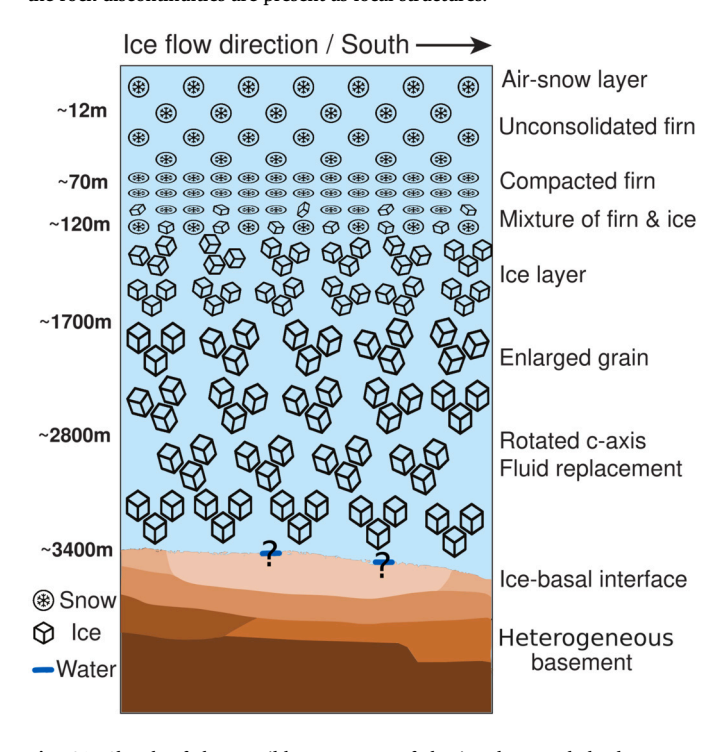


Fig. 10. Sketch of the possible structures of the ice-sheet and the basement revealed by seismic waves.

of bed reflections to uncover the petrophysical properties of associated englacial discontinuities.

7. Conclusions

We observe a series of seismic waves from an active-source acquisition in the west Antarctic. The methods we use can be applied to a variety of subsurface structures where there is a near-surface low-velocity zone on top of a higher velocity zone, such as an ice sheet with shallow firn or a critical zone environment with shallow unconsolidated sediment. The joint leaky and normal modes dispersion curve inversion returns an estimation for both P- and S-wave velocities in the near-surface. The velocities themselves and their ratios are key to understanding the fine structures of the ice sheet and inferring the petrophysics of the shallow firn and ice. Different from the previous studies, we observe strong *PP* and weak *PS* englacial reflections at lower

frequencies and show a much cleaner seismic image of layer boundaries. The ice sheet near the basement exhibits multiple continuous and nearly flat layers, indicating a heterogeneous composition of the deep ice sheet. We attribute the englacial reflectivity to variations in c-axis orientation and fluid replacement in the porous ice. Our reverse-time migration seismic image indicates a rugged topography of the ice-basal interface, and heterogeneous bedrock with faults may exist. In the future, we plan to examine the material properties of the ice sheet in more detail, including looking for evidence of liquid water.

Code availability

The numerical solver for seismic wavefield extrapolation and inversion (SPECFEM2D) is available at https://github.com/geodynamics/specfem2d. We also use Madagascar to process the data and calculate the Kirchhoff migration image (https://www.reproducibility.org/wiki/Main Page).

CRediT authorship contribution statement

Zhendong Zhang: Writing – original draft, Methodology, Formal analysis, Conceptualization. Nori Nakata: Writing – review & editing, Supervision, Methodology, Funding acquisition. Marianne Karplus: Writing – review & editing, Supervision, Investigation, Funding acquisition. Galen Kaip: Writing – review & editing, Funding acquisition. Lei Qin: Writing – review & editing, Methodology. Zhengbo Li: Writing – review & editing, Methodology. Caiwang Shi: Writing – review & editing, Methodology. Xiaofei Chen: Writing – review & editing, Methodology.

Declaration of competing interest

All authors disclosed no relevant relationships.

Data availability

The waveform data used in this study can be downloaded from the IRIS Data Management Center (available at https://ds.iris.edu/mda/2E/#2E_2018-01-01_2019-12-31). The 15 arc-second global relief is available at https://www.generic-mapping-tools.org/remote-datasets/earth-relief.html. The borehole sonic log data are available at https://nsidc.org/data/nsidc-0592/versions/1.

Acknowledgements

We thank the High Performance Computing (HPC) team at King Abdullah University of Science and Technology (KAUST) for providing guidance on using IBEX and Shaheen clusters. The computing for this project was partly performed at the University of Oklahoma (OU) Supercomputing Center for Education & Research (OSCER). This work is from the Thwaites Interdisciplinary Margin Evolution (TIME) project, a component of the International Thwaites Glacier Collaboration (ITGC). Support from National Science Foundation (NSF: OPP-1739027) and Natural Environment Research Council (NERC: Grant NE/S006788/1). Logistics provided by NSF-U.S. Antarctic Program and NERC-British Antarctic Survey. ITGC Contribution No. ITGC-107. Zhendong Zhang is partially supported by the CAS Pioneer Hundred Talents Program.

Appendix A. Supplementary material

Supplementary material related to this article can be found online at https://doi.org/10.1016/j.epsl.2024.118701.

References

- Artemieva, I.M., Thybo, H., 2020. Continent size revisited: geophysical evidence for West Antarctica as a back-arc system. Earth-Sci. Rev. 202, 103106.
- Bamber, J.L., Riva, R.E., Vermeersen, B.L., LeBrocq, A.M., 2009. Reassessment of the potential sea-level rise from a collapse of the West Antarctic Ice Sheet. Science 324, 901–903
- Battle, M., Severinghaus, J., Sofen, E., Plotkin, D., Orsi, A., Aydin, M., Montzka, S., Sowers, T., Tans, P., 2011. Controls on the movement and composition of firn air at the West Antarctic Ice Sheet Divide. Atmos. Chem. Phys. 11, 11007–11021.
- Bentley, C.R., 1971. Seismic Anisotropy in the West Antarctic Ice Sheet. Antarctic Snow and Ice Studies II, vol. 16, pp. 131–177.
- Bentley, C.R., 1975. Advances in geophysical exploration of ice sheets and glaciers. J. Glaciol. 15, 113–135.
- Chaput, J., Aster, R., Karplus, M., Nakata, N., 2022. Ambient high-frequency seismic surface waves in the firn column of central West Antarctica. J. Glaciol.. 1–14.
- Clyne, E.R., Anandakrishnan, S., Muto, A., Alley, R.B., Voigt, D.E., 2020. Interpretation of topography and bed properties beneath Thwaites Glacier, West Antarctica using seismic reflection methods. Earth Planet. Sci. Lett. 550, 116543.
- Diez, A., Eisen, O., Weikusat, I., Eichler, J., Hofstede, C., Bohleber, P., Bohlen, T., Polom, U., 2014. Influence of ice crystal anisotropy on seismic velocity analysis. Ann. Glaciol. 55. 97–106.
- Duffaut, K., Landrø, M., 2007. Vp/Vs ratio versus differential stress and rock consolidation — a comparison between rock models and time-lapse AVO data. Geophysics 72, C81–C94.
- Eisen, O., Hofstede, C., Diez, A., Kristoffersen, Y., Lambrecht, A., Mayer, C., Blenkner, R., Hilmarsson, S., 2015. On-ice vibroseis and snowstreamer systems for geoscientific research. Polar Sci. 9, 51–65.
- ETOPO, 2022. ETOPO 2022 15 arc-second global relief model. In: NOAA National Centers for Environmental Information. NOAA Boulder, CO, USA.
- Fitzpatrick, J.J., Voigt, D.E., Fegyveresi, J.M., Stevens, N.T., Spencer, M.K., Cole-Dai, J., Alley, R.B., Jardine, G.E., Cravens, E.D., Wilen, L.A., et al., 2014. Physical properties of the WAIS divide ice core. J. Glaciol. 60, 1181–1198.
- Foti, S., Hollender, F., Garofalo, F., Albarello, D., Asten, M., Bard, P.Y., Comina, C., Cornou, C., Cox, B., Di Giulio, G., et al., 2018. Guidelines for the good practice of surface wave analysis: a product of the InterPACIFIC project. Bull. Earthq. Eng. 16, 2367–2420.
- Fu, L., Guo, J., Chen, X., 2021a. Measurement of ice flow velocities from GPS positions logged by short-period seismographs in East Antarctica. Sci. China Earth Sci. 64, 1381–1389.
- Fu, L., Guo, J., Li, J., Deng, B., Liu, G., Xiao, E., Chen, X., 2021b. Imaging the ice sheet and uppermost crustal structures with a dense linear seismic array in the Larsemann Hills, Prydz Bay, East Antarctica. Seismol. Res. Lett. 93, 288–295.
- Gao, L., Xia, J., Pan, Y., 2014. Misidentification caused by leaky surface wave in high-frequency surface wave method. Geophys. J. Int. 199, 1452–1462.
- Halliday, D., Curtis, A., 2008. Seismic interferometry, surface waves and source distribution. Geophys. J. Int. 175, 1067–1087.
- Han, D.h., Nur, A., Morgan, D., 1986. Effects of porosity and clay content on wave velocities in sandstones. Geophysics 51, 2093–2107.
- Holland, C.W., Anandakrishnan, S., 2009. Subglacial seismic reflection strategies when source amplitude and medium attenuation are poorly known. J. Glaciol. 55, 931–937.
- Horgan, H., Anandakrishnan, S., Alley, R.B., Peters, L., Tsoflias, G.P., Voigt, D., Winberry, J., 2008. Complex fabric development revealed by englacial seismic reflectivity: Jakobshavn Isbræ, Greenland. Geophys. Res. Lett. 35.
- Horgan, H.J., Anandakrishnan, S., Alley, R.B., Burkett, P.G., Peters, L.E., 2011. Englacial seismic reflectivity: imaging crystal-orientation fabric in West Antarctica. J. Glaciol. 57, 639–650.

- Jordan, T.A., Thompson, S., Kulessa, B., Ferraccioli, F., 2023. Geological sketch map and implications for ice flow of Thwaites glacier, West Antarctica, from integrated aerogeophysical observations. Sci. Adv. 9, eadf2639.
- Joughin, I., Tulaczyk, S., Bamber, J.L., Blankenship, D., Holt, J.W., Scambos, T., Vaughan, D.G., 2009. Basal conditions for Pine Island and Thwaites Glaciers, West Antarctica, determined using satellite and airborne data. J. Glaciol. 55, 245–257.
- Karplus, M.S., Kaip, G., Harder, S.H., Veitch, S.A., Nakata, N., Booth, A.D., Walter, J.I., Christoffersen, P., Tulaczyk, S.M., 2019. Surface explosives in active-source seismic surveying: performance and new imaging at the West Antarctic Ice Sheet Divide. In: AGU Fall Meeting Abstracts, NS13A-03.
- King, M.A., Altamimi, Z., Boehm, J., Bos, M., Dach, R., Elosegui, P., Fund, F., Hernández-Pajares, M., Lavallee, D., Mendes Cerveira, P.J., et al., 2010. Improved constraints on models of glacial isostatic adjustment: a review of the contribution of ground-based geodetic observations. Surv. Geophys. 31, 465–507.
- Kornei, K., 2020. Controlled explosions pave the way for Thwaites Glacier research. In:
- Koutnik, M.R., Fudge, T., Conway, H., Waddington, E.D., Neumann, T.A., Cuffey, K.M., Buizert, C., Taylor, K.C., 2016. Holocene accumulation and ice flow near the West Antarctic Ice Sheet Divide ice core site. J. Geophys. Res., Earth Surf. 121, 907–924.
- Lai, C.Y., Kingslake, J., Wearing, M.G., Chen, P.H.C., Gentine, P., Li, H., Spergel, J.J., van Wessem, J.M., 2020. Vulnerability of Antarctica's ice shelves to meltwater-driven fracture. Nature 584, 574–578.
- Li, Z., Shi, C., Chen, X., 2021. Constraints on crustal P wave structure with leaking mode dispersion curves. Geophys. Res. Lett. 48, e2020GL091782.
- Li, Z., Shi, C., Ren, H., Chen, X., 2022. Multiple leaking mode dispersion observations and applications from ambient noise cross-correlation in Oklahoma. Geophys. Res. Lett. 49, e2021GL096032.
- Lloyd, A.J., Wiens, D.A., Zhu, H., Tromp, J., Nyblade, A.A., Aster, R.C., Hansen, S.E., Dalziel, I.W., Wilson, T.J., Ivins, E.R., et al., 2020. Seismic structure of the Antarctic upper mantle imaged with adjoint tomography. J. Geophys. Res., Solid Earth 125.
- Meredith, M., Sommerkorn, M., Cassotta, S., Derksen, C., Ekaykin, A., Hollowed, A., Kofinas, G., Mackintosh, A., Melbourne-Thomas, J., Muelbert, M., et al., 2019. IPCC special report on the ocean and cryosphere in a changing climate. In: Polar Regions. Chapter 3.
- Morlighem, M., 2022. MEaSUREs BedMachine Antarctica, Version 3. NASA National Snow and Ice Data Center Distributed Active Archive Center.
- Muto, A., Anandakrishnan, S., Alley, R.B., Horgan, H.J., Parizek, B.R., Koellner, S., Christianson, K., Holschuh, N., 2019. Relating bed character and subglacial morphology using seismic data from Thwaites Glacier, West Antarctica. Earth Planet. Sci. Lett. 507, 199–206
- Oliver, J., Major, M., 1960. Leaking modes and the PL phase. Bull. Seismol. Soc. Am. 50, 165–180.
- Parizek, B., Christianson, K., Anandakrishnan, S., Alley, R., Walker, R., Edwards, R., Wolfe, D., Bertini, G., Rinehart, S., Bindschadler, R., et al., 2013. Dynamic (in) stability of Thwaites Glacier, West Antarctica. J. Geophys. Res., Earth Surf. 118, 638–655.
- Peters, L.E., Anandakrishnan, S., Alley, R.B., Winberry, J.P., Voigt, D.E., Smith, A.M., Morse, D.L., 2006. Subglacial sediments as a control on the onset and location of two Siple Coast ice streams, West Antarctica. J. Geophys. Res., Solid Earth 111.
- Phạm, T.S., Tkalčić, H., 2021. Constraining floating ice shelf structures by spectral response of teleseismic P-wave coda: Ross Ice Shelf, Antarctica. J. Geophys. Res., Solid Earth 126, e2020JB021082.
- Ringler, A.T., Anthony, R.E., Karplus, M.S., Holland, A.A., Wilson, D.C., 2018. Laboratory tests of three Z-Land Fairfield Nodal 5-Hz, Three-Component Sensors. Seismol. Res. Lett. 89, 1601. https://doi.org/10.1785/0220170236.
- Roth, M., Holliger, K., Green, A., 1998. Guided waves in near-surface seismic surveys. Geophys. Res. Lett. 25. 1071–1074.
- Scherer, R.P., Aldahan, A., Tulaczyk, S., Possnert, G., Engelhardt, H., Kamb, B., 1998.
 Pleistocene collapse of the West Antarctic ice sheet. Science 281, 82–85.
- Schröder, C.T., Scott Jr., W.R., 2001. On the complex conjugate roots of the Rayleigh equation: the leaky surface wave. J. Acoust. Soc. Am. 110, 2867–2877.
- Shearer, P.M., 2019. Introduction to Seismology. Cambridge University Press, Cambridge. Shen, W., Wiens, D.A., Anandakrishnan, S., Aster, R.C., Gerstoft, P., Bromirski, P.D.,
- Hansen, S.E., Dalziel, I.W., Heeszel, D.S., Huerta, A.D., et al., 2018. The crust and upper mantle structure of central and West Antarctica from Bayesian inversion of Rayleigh wave and receiver functions. J. Geophys. Res., Solid Earth 123, 7824–7849.
- Shi, C., Ren, H., Li, Z., Chen, X., 2022. Calculation of normal and leaky modes for horizontal stratified models based on a semi-analytical spectral element method. Geophys. J. Int. 230, 1928–1947.
- Siegert, M.J., Carter, S., Tabacco, I., Popov, S., Blankenship, D.D., 2005. A revised inventory of Antarctic subglacial lakes. Antarct. Sci. 17, 453–460.
- Smith, A., 1996. Ice shelf basal melting at the grounding line, measured from seismic observations. J. Geophys. Res., Oceans 101, 22749–22755.
- Wang, C., Wang, Y., 2017. Ground roll attenuation using polarization analysis in the t-f-k domain. Geophys. J. Int. 210, 240–254.
- Wiens, D.A., Shen, W., Lloyd, A.J., 2022. The Seismic Structure of the Antarctic Upper Mantle, vol. 56. Geological Society, London, Memoirs, M56-2020.
- Wittlinger, G., Farra, V., 2012. Observation of low shear wave velocity at the base of the polar ice sheets: evidence for enhanced anisotropy. Geophys. J. Int. 190, 391–405.

- $Wittlinger, G., Farra, V., 2015. \ Evidence of unfrozen liquids and seismic anisotropy at the base of the polar ice sheets. Polar Sci. 9, 66–79.$
- Xia, J., Miller, R.D., Park, C.B., 1999. Estimation of near-surface shear-wave velocity by inversion of Rayleigh waves. Geophysics 64, 691–700.
- Young, T.J., Martín, C., Christoffersen, P., Schroeder, D.M., Tulaczyk, S.M., Dawson, E.J., 2021. Rapid and accurate polarimetric radar measurements of ice crystal fabric orientation at the Western Antarctic Ice Sheet (WAIS) Divide ice core site. Cryosphere 15, 4117–4133.
- Zhang, Z., Nakata, N., Karplus, M., Kaip, G., Yi, J., 2022. Shallow ice-sheet composite structure revealed by seismic imaging near the West Antarctic Ice Sheet (WAIS) Divide Camp. J. Geophys. Res., Earth Surf. 127.
- Zhang, Z.D., Alkhalifah, T., 2019. Wave-equation Rayleigh-wave dispersion inversion using fundamental and higher modes. Geophysics 84, EN57–EN65.
- Zheng, Y., Hu, H., 2021. Surface wave prediction and removal from seismic data. US Patent App. 17/267,555.